ADVANCED MATERIALS
www.advmat.de

Hot-Pressing Metal Covalent Organic Frameworks as Personal Protection Films

Jiajia Wang, Li Li, Chuanshan Xu, Hong Jiang, Qin-Xie Xie, Xin-Yi Yang, Ji-Cheng Li, Huiying Xu, Yifa Chen, Wei Yi,* Xu-Jia Hong,* and Ya-Qian Lan*

Effective personal protection is crucial for controlling infectious disease spread. However, commonly used personal protective materials such as disposable masks lack antibacterial/antiviral function and may lead to cross infection. Herein, a polyethylene glycol-assisted solvent-free strategy is proposed to rapidly synthesize a series of the donor–acceptor metal-covalent organic frameworks (MCOFs) (i.e., GZHMU-2, JNM-1, and JNM-2) under air atmosphere and henceforth extend it via in situ hot-pressing process to prepare MCOFs based films with photocatalytic disinfect ability. Best of them, the newly designed GZHMU-2 has a wide absorption spectrum (200 to 1500 nm) and can efficiently produce reactive oxygen species under sunlight irradiation, achieving excellent photocatalytic disinfection performance. After in situ hot-pressing as a film material, the obtained GZHMU-2/NMF can effectively kill *E. coli* (99.99%), *S. aureus* (99%), and H1N1 (92.5%), meanwhile possessing good reusability. Noteworthy, the long-term use of a GZHMU-2/NWF-based mask has verified no damage to the living body by measuring the expression of mouse blood routine, lung tissue, and inflammatory factors at the in-vivo level.

1. Introduction

Pathogenic microorganism infection is an increasingly serious public health problem that threatens human life.[1,2] New microbial infections such as influenza virus, Ebola virus, MERS-CoV, and COVID-19 continue to occur, bringing great disasters to society.[3,4] Airborne transmission is the main route for bacteria and virus spread, which can form aerosols to stay in the air or carrier surface for a long time, thus causing rapid disease spread.[5–7] Avoiding pathogen transmission by wearing masks and protective clothing can effectively protect individuals from infection.[8,9] However, significant disadvantages exist for these currently used disposable masks: 1) limited self-cleaning ability; 2) promoting microbial attachment and reproduction; 3) environmental/resource issues. Thus, there is an urgent need to develop composite protective materials to address these challenges. Meanwhile, the reactive oxygen species (ROS) generated by photocatalysis, such as hydroxyl radicals, superoxide anions, and singlet oxygen, can strongly interact with microorganisms, causing oxidative stress in them and inactivating them through oxidative degradation of biological macromolecules.[10–12] Despite some functional materials with photocatalytic antibacterial/antiviral properties have been reported,[13–17] novel materials that can be facilely processed into film materials and fitted into protective materials such as masks and protective clothing to realize the photocatalytic disinfection of microorganisms are still highly demanded yet largely unmet.

In recent years, porous crystalline materials, such as metal–organic frameworks (MOFs)[18–20] or covalent organic frameworks (COFs),[21–23] have shown strong flexibility in tuning the specific surface area, pore structure, and pore chemical environment by the specific design of structure struts, making them have unique advantages in gas adsorption, photocatalysis or bio-applications, etc.[24–29] Metal covalent organic frameworks (MCOFs), as a new type of porous material, draw on the design

J. Wang, L. Li, C. Xu, H. Jiang, Q.-X. Xie, X.-Y. Yang, J.-C. Li, H. Xu, W. Yi, X.-J. Hong
The Fifth Affiliated Hospital
Guangdong Provincial Key Laboratory of Molecular Target & Clinical Pharmacology, NMPA and State Key Laboratory of Respiratory Disease
School of Pharmaceutical Sciences
School of Public Health
Guangzhou Medical University
Guangzhou 511436, China
E-mail: yiwei@gzhmu.edu.cn; hongxujia@gzhmu.edu.cn

Y. Chen, Y.-Q. Lan
National and Local Joint Engineering Research Center of MPTES in High Energy and Safety LIBs
Engineering Research Center of MTEES (Ministry of Education)
Key Lab. of ETESPG(GHEI)
School of Chemistry
South China Normal University
Guangzhou 510006, P. R. China
E-mail: 20200698@m.scnu.edu.cn

The ORCID identification number(s) for the author(s) of this article can be found under https://doi.org/10.1002/adma.202311519

DOI: 10.1002/adma.202311519

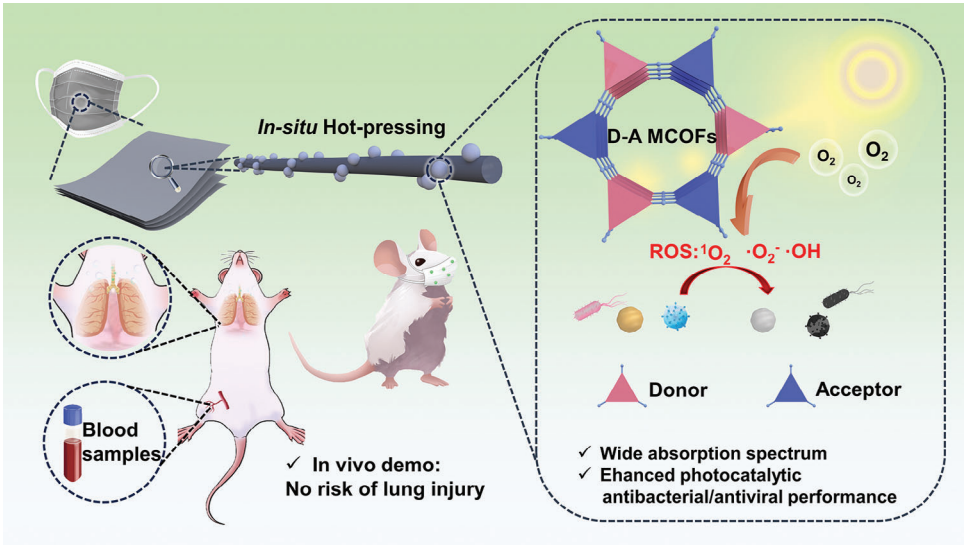

Scheme 1. Schematic illustration of donor–acceptor MCOF-based film with high photocatalytic antibacterial/antiviral efficiency for protective materials.

concept of MOFs and COFs that can integrate their advantages together.[30–33] They not only enrich the types of porous framework materials but also provide a good platform for the reasonable design of efficient photocatalytic materials.[34,35] In particular, compared with traditional photocatalytic materials such as metal oxides and metal sulfides, MCOFs have the following advantages: 1) through reasonable design of organic monomers, the absorption spectrum of the MCOFs can be well-optimized; 2) the organic ligands can effectively separate the metal nodes, thereby improving the utilization rate of active sites; 3) the abundant porous structure is conducive to ROS diffusion, improving the efficiency of producing ROS.[36–40] However, up to date, only a few cases of MOFs or COFs based composite films with photocatalytic antibacterial/antiviral activity have been gradually reported for effective personal protection, the absorption spectra of these materials are still difficult to cover the whole visible region, and some important issues like biosafety, processability, and the photocatalytic efficiency still need to be further improved.[41,29] Additionally, during the use of photocatalytic, nanomaterials may detach from the composite film and enter the human lung through breathing when wearing for a long time, causing damage to the human body, thus the potential health effects of these released nanomaterials in vivo should also be taken into account to promote subsequent practical applications. In this regard, it would be much necessary to design advanced photocatalytic antibacterial/antiviral materials like MCOFs with good biocompatibility, easy processing properties, and wide absorption spectrum that can meet the high requirements of personal protection, yet such powerful materials have been rarely reported.

Based on the above considerations, herein, we have developed a polyethylene glycol (PEG) assisted solvent-free strategy to rapidly synthesize a series of the donor–acceptor MCOFs (i.e., GZHMU-2, JNM-1, and JNM-2) under air atmosphere, and henceforth extend it via in situ hot-pressing process to prepare MCOFs based film with photocatalytic disinfect ability (**Scheme 1**). Best of them, the newly designed GZHMU-2 has a wide absorption spectrum and can efficiently produce ROS under sunlight irradiation, achieving excellent photocatalytic disinfection performance. By hot pressing, GZHMU-2 was further in situ grown on the non-woven fabric (NWF) to prepare a composite film, GZHMU-2/NMF. After 30 min of sunlight exposure, the obtained GZHMU-2/NMF can effectively kill 99.99% of *Escherichia coli* (*E. coli*), 99% of *Staphylococcus aureus* (*S. aureus*), as well as 92.5% of H1N1. The GZHMU-2/NMF-based air filters show remarkable performance for comprehensive sterilization of air and the GZHMU-2/NWF-based mask demonstrates more advantages in preventing pathogens than commercial masks. In addition, for the first time, we comprehensively studied the in vivo toxicity of the frame-based film material by measuring the expression of mouse blood routine, lung tissue, and inflammatory factors. The results showed that the composite film material had good biosafety and stability in vivo, which laid the foundation for further practical application.

2. Results

2.1. Synthesis and Characterization of Cu_3-Based MCOFs

As shown in **Figure 1a**, in order to grow MCOFs onto NWF later, we choose to use *p*-toluenesulfonic acid (PTSA) as catalyst and PEG as assisted agent to react donor organic monomer (i.e., 2,4,6-tris(4-aminophenyl))−1,3,5-trianiline (TAPT), 1,3,5-tris(4-aminophenyl)benzene (TAPB) and Tris(4-aminophenyl) amine (TAPA) with Cu_3 directly at 170 °C for 30 min under air atmosphere to obtain series MCOFs, that is, JNM-1, JNM-2, and GZHMU-2, respectively (detail see Methods). Materials Studio was used to simulate the structure of GZHMU-2 and further combined with Pawley refinements to fit the eclipsed and staggered model parameters with the powder X-ray diffraction (PXRD) data (Figure 1a–c). The results show that GZHMU-2 exists in AA stacking model with fitting cell parameters of $a = b = 21.8636$ Å, $c = 3.4721$ Å ($R_{wp} = 4.00\%$, $R_p = 3.20\%$) (Tables S1,S2, Supporting Information). The peaks at 4.53° and 7.93° can be attributed to the crystal planes of (100) and (110), respectively (Figure 1c). At the same time, for the subsequent comparison of antibacterial activity, we also synthesized Cu-free

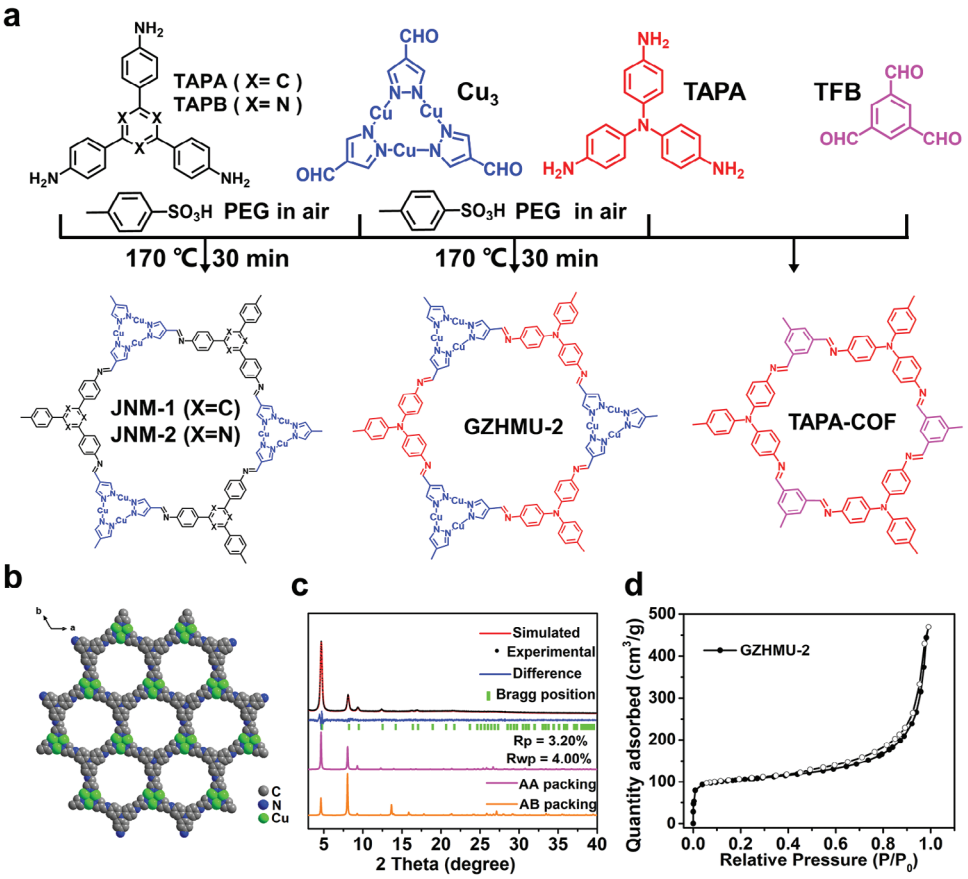

Figure 1. Synthesis and characterization of series donor–acceptor MCOFs based on Cu3 and TAPA-COF. a) Synthesis and structure diagram of the series donor–acceptor MCOFs based on Cu3 and TAPA-COF. b) Structure of GZHMU-2 view along the c axis. c) Experimental and Pawley-refined patterns of GZHMU-2. d) N2 sorption curves of GZHMU-2.

COF, TAPA-COF, according to the references.[42] As shown in Figures S1,S2 (Supporting Information), the PXRD patterns of synthesized JNM-1, JNM-2 and TAPA-COF match well with the reported ones.[42,43] For JNM-1 and JNM-2, the diffraction peaks at 4.22° and 7.36° can be attributed to the crystal planes of (100) and (110), respectively, which proves that the PEG asssisted solvent-free strategy can successfully synthesize MCOFs based on Cu_3 in the air.[39] In addition, the porosity and surface area of JNM-1, JNM-2, and GZHMU-2 were measured at 77 K through N_2 adsorption–desorption measurements (Figure 1d; Figure S3, Supporting Information). The Brunauer–Emmett–Teller surface area of GZHMU-2 was examined to be 358 m^2 g^{-1}. It is interesting to note that, due to the absence of inert gas protection in the synthesis process, X-ray photoelectron spectroscopy spectra show that the valence of Cu in JNM-1, JNM-2, and GZHMU-2 has a mixed valence of +1 and +2, which might be due to that Cu^+ in Cu_3 node is partially oxidized by air (Figure S4, Supporting Information).[43]

2.2. Photocatalytic Properties and Mechanisms

To demonstrate that this series of Cu_3-based MCOFs has a donor–acceptor electronic structure (**Figure** 2a), we investigated the frontier molecular orbitals of the repeating units in the MCOFs using density functional theory (DFT) calculations. As shown in Figure 2b,c and Figure S5 (Supporting Information), the highest occupied molecular orbital (HOMO) and lowest unoccupied molecular orbital (LUMO) values of GZHMU-2 (HOMO, −4.36 eV and LUMO, −1.13 eV), JNM-1 (−5.20 and −1.46 eV) and JNM-2 are calculated. The corresponding band gaps (E_g) are 3.23, 3.74, and 3.77 eV for GZHMU-2, JNM-1 and JNM-2, respectively. The results show that the LUMO of the three MCOFs is almost the same, which mainly comes from the contribution of the Cu_3 node, indicating that the Cu_3 node mainly acts as the acceptor in these three MCOFs. As for HOMO orbitals, the figure shows that the HOMO orbitals of these three MCOFs are mainly derived from the amino bonding functional groups. The difference is that TAPA contributes the most to HOMO, resulting in the lowest band gap of GZHMU-2 unit. This result can be attributed to the fact that TAPA has a stronger electron-donating ability than TAPB and TAPT. The DFT calculation results show that GZHMU-2, JNM-1, and JNM-2 have donor–acceptor structure, while the band structure of GZHMU-2 can be effectively adjusted and its absorption spectrum can be expanded by adjusting the electron donor unit.

In addition, we tested UV–vis absorption spectra of series MCOFs and TAPA-COF. As shown in Figure 2d, compared with the framework containing the Cu_3 node, the absorption of TAPA-COF is significantly weaker than GZHMU-2. In the series of

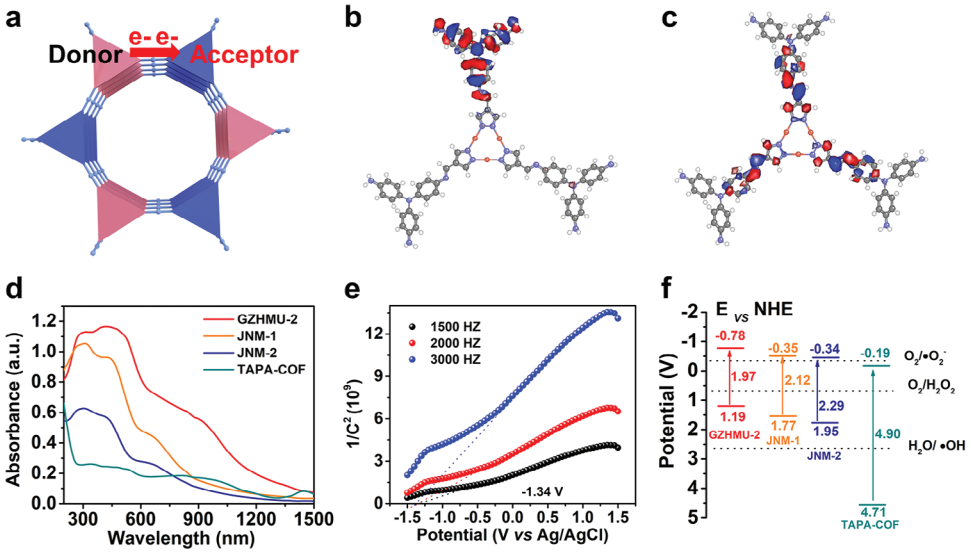

Figure 2. Photocatalytic properties and DFT calculations. a) Scheme of the donor–acceptor units in the Cu_3-based MCOF. b) HOMO and c) LUMO surface plots (isovalue = 0.025) from DFT calculations for the units in GZHMU-2. d) UV–vis absorption spectra of GZHMU-2, JNM-1, JNM-2 and TAPA-COF. e) Mott–Schottky plot of GZHMU-2. f) Band-structure diagram.

Cu_3-based MCOFs, the absorption spectra of JNM-2, JNM-1, and GZHMU-2 are gradually redshifted, which can be attributed to the gradual enhancement of electron-donating ability of TAPT, TAPB, and TAPA, thus broadening the absorption spectra of donor–acceptor MCOFs gradually. Remarkably, the light absorption range of GZHMU-2 is from 200 to 1500 nm, which basically covers the normal light wavelength. It is shown that the transient photocurrent response intensity of GZHMU-2 is much higher than those of TAPA-COF, JNM-1, and JNM-2 (Figure S6, Supporting Information). In addition, Mott–Schottky measurements were performed at the frequencies of 1500, 2000, and 3000 Hz to analyze the energy band position of GZHMU-2, JNM-1, JNM-2, and TAPA-COF. As shown in Figure 2e, GZHMU-2 demonstrates n-type semiconductor property, from which the flat band position of GZHMU-2 was determined to be −0.78 eV vs NHE (equal to the conduction band (CB)). The experimental band gap of the materials can be calculated according to the absorption spectrum. Accordingly, the experimental energy bandgap (E_g) GZHMU-2, JNM-1, JNM-2, and TAPA-COF were evaluated to be 1.97, 2.12, 2.29, and 4.90 eV by their Tauc plots, respectively (Figure 2f; Figure S7, Supporting Information). According to the equation $E_g = E_{VB} - E_{CB}$, the valence band (VB) position of GZHMU-2 was then calculated to be 1.19 eV vs NHE (Figure 2f). Likewise, the CB of JNM-1, JNM-2, and TAPA-COF were determined to be −0.35, −0.34, and −0.19 eV (vs NHE), respectively (Figure S8, Supporting Information). Meanwhile, the VB positions of JNM-1, JNM-2, and TAPA-COF were 1.77, 1.95, and 4.71 eV (vs NHE), respectively. Based on the above results, the band positions of GZHMU-2, JNM-1, JNM-2, TAPA-COF, as well as with ROS generation potential were demonstrated in Figure 2f. Apparently, compared to these other materials, GZHMU-2 has more thermodynamic advantages in the photocatalytic production of ROS.

In general, the antibacterial/antiviral performance of photocatalytic materials is mainly attributed to the generation of ROS.[25,41] Therefore, the types of ROS generated during the photocatalytic process were systematically investigated. Specifically, in electron paramagnetic resonance (EPR) determination, $\cdot O_2^-$ and ·OH can be determined by 5,5-dimethylpyrroline N-oxide (DMPO) (Figures S9,S10, Supporting Information), while $^1O_2$ can be determined by 2,2,6,6-Tetramethyl-4-piperidone hydrochloride(TEMP) radical spin catcher (Figure S11, Supporting Information). Upon light excitation, characteristic peaks of typical DMPO-$\cdot O_2^-$, DMPO-·OH, and TEMP-$^1O_2$ adducts can be clearly observed for GZHMU-2, JNM-1, and JNM-2. In sharp contrast, silent EPR spectra were observed for all unirradiated samples, suggesting the vital role of light illumination during these processes. This result can also be explained from the energy level distribution diagram. As shown in Figure 2f, we can see that the band structures of GZHMU-2, JNM-1, and JNM-2 are sufficient to reduce the surface adsorbed O_2 to $\cdot O_2^-$ (−0.33 V vs NHE). Among them, GZHMU-2 has the lowest band gap and wider light absorption range, making GZHMU-2 the best photocatalytic activity. However, TAPA-COF has a large band gap and mismatched energy levels, so it cannot produce ROS. Although ·OH was detected in the process, it is obvious that the electronic band structure of GZHMU-2, JNM-1, and JNM-2 are sufficient to reduce the surface adsorbed O_2 to H_2O_2 (−0.67 V vs NHE), but insufficient to meet the requirements for the synthesis of ·OH ($H_2O/\cdot OH$ = +2.68 V vs NHE). To investigate the mechanism of ·OH, *p*-hydroxyphenylacetic acid is used as an H_2O_2 probe to verify the process. As shown in Figure S12 (Supporting Information), it can be seen that H_2O_2 was generated in the presence of TAPA-COF, while the other materials are exactly the opposite. We speculate that one possible mechanism is that GZHMU-2, JNM-1, and JNM-2 contain active metal sites, Cu^+, which can lead to Fenton-like reactions, effectively converting the generated hydrogen peroxide into ·OH (**Figure** 3a). Though the electronic band structure of TAPA-COF is sufficient to oxidize the surface adsorbed H_2O to ·OH ($H_2O/\cdot OH$ = +2.68 vs NHE), due to the

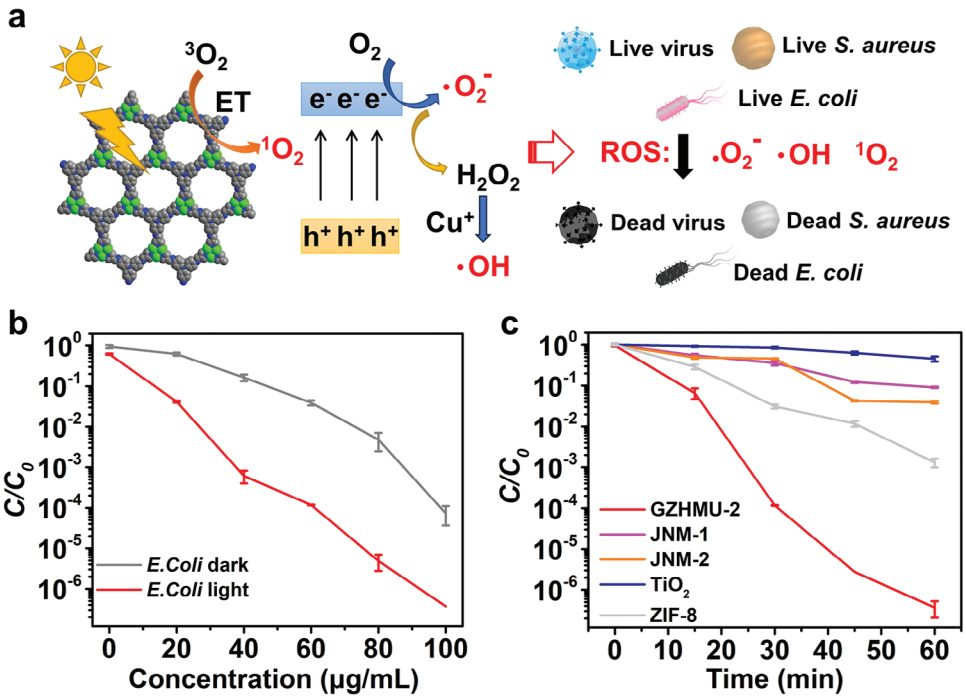

Figure 3. Photocatalytic disinfection performance of GZHMU-2. a) Photocatalytic disinfection mechanism of GZHMU-2. b) Photocatalytic disinfection efficiency of GZHMU-2 against *E. coli* at different dosage levels. c) Disinfection performance comparison among GZHMU-2, JNM-1, JNM-2, ZIF-8 and TiO_2 against *E. coli*.

large band gap of TAPA-COF, the electron transition and transfer are blocked, making ·OH basically undetectable, which can also explain why singlet oxygen cannot be produced by TAPA-COF under light (Figure S10, Supporting Information). For the series of MCOFs, due to the appropriate bandgap width, the energy can be transferred under light, thus producing $^1O_2$ (Figure S11, Supporting Information, Figure 3a). The above theoretical calculation and experimental results show that GZHMU-2 has the widest light absorption range and a suitable band gap, which enables it to efficiently produce abundant ROS (i.e., $^1O_2$, ·OH, and $\cdot O_2^-$) under simulated sunlight, so as to be used for the photocatalytic killing of microorganisms (Figure 3a).

2.3. Photocatalytic Antibacterial Performance of GZHMU-2

The photocatalytic antibacterial efficiency of the synthesized donor–acceptor MCOFs materials (GZHMU-2, JNM-1, and JNM-2) was examined, using *E. coli* as the model bacteria. The antibacterial experiments were carried out in 0.9% (w/v) saline, using a hand-held xenon lamp (power density: 110 mW cm^{-2}) with an AM 1.5 filter and attenuation plate (300 nm < λ < 1100 nm) as the light source. The initial concentration of *E. coli* was 10^7 colony-forming unit (CFU) mL^{-1}. First, the photocatalytic disinfection performance of GZHMU-2 on *E. coli* at different dosage levels was performed. As shown in Figure 3b, after 30 min of light irradiation, the bacterial survival rate dramatically decreased with increased dosage of GZHMU-2. When the concentration of GZHMU-2 is only 60 μg mL^{-1}, the bactericidal rate of *E. coli* can reach up to 99.99%. *E. coli* inactivation efficiencies of over 99.9999% were achieved as the catalyst dosage was increased to 100 μg mL^{-1}. Encouraged by these results, we further investigated the antibacterial activity of GZHMU-2 on *S. aureus*. When the dosage of GZHMU-2 was 100 μg mL^{-1}, a 99.99% reduction of *S. aureus* can also be obtaining (Figure S13, Supporting Information). Specifically, in order to confirm the superior photocatalytic antibacterial performance of GZHMU-2, systematic comparative tests were carried out among JNM-1, JNM-2, representative ZIF-8,[41] and the traditional semiconductive photocatalyst anatase (TiO_2) with a concentration of 60 μg mL^{-1}. As shown in Figure 3c and Table S3 (Supporting Information), GZHMU-2 has exhibited absolute superiority in antibacterial performance compared to other photocatalytic materials. Note, after ≈30 min of illumination, the antibacterial rate of GZHMU-2 is up to 99.99%, three orders of magnitude higher than that of ZIF-8 with only ≈90%. The above results clearly illustrated that the novel donor–acceptor MCOF, GZHMU-2, exhibits excellent photocatalytic antibacterial properties.

Furthermore, systematic experiments were performed to further confirm the light-induced antibacterial ability of GZHMU-2 in detail. Excitingly, the zeta potential of GZHMU-2 was completely opposite to that of bacteria, which could further facilitate the interaction process with bacteria through electrostatic interactions (Figure S14, Supporting Information). As shown in Figure S15 (Supporting Information), the PXRD pattern showed that the framework of GZHMU-2 still exists after photocatalysis, indicating that it has good stability. In Addition, to confirm the successful antibacterial interaction, the morphology of bacteria before and after interaction with GZHMU-2 was characterized by transmission electron microscopy (TEM). With the necessary conditions, including GZHMU-2 and light irradiation, it can be observed that the cell membrane of bacteria was

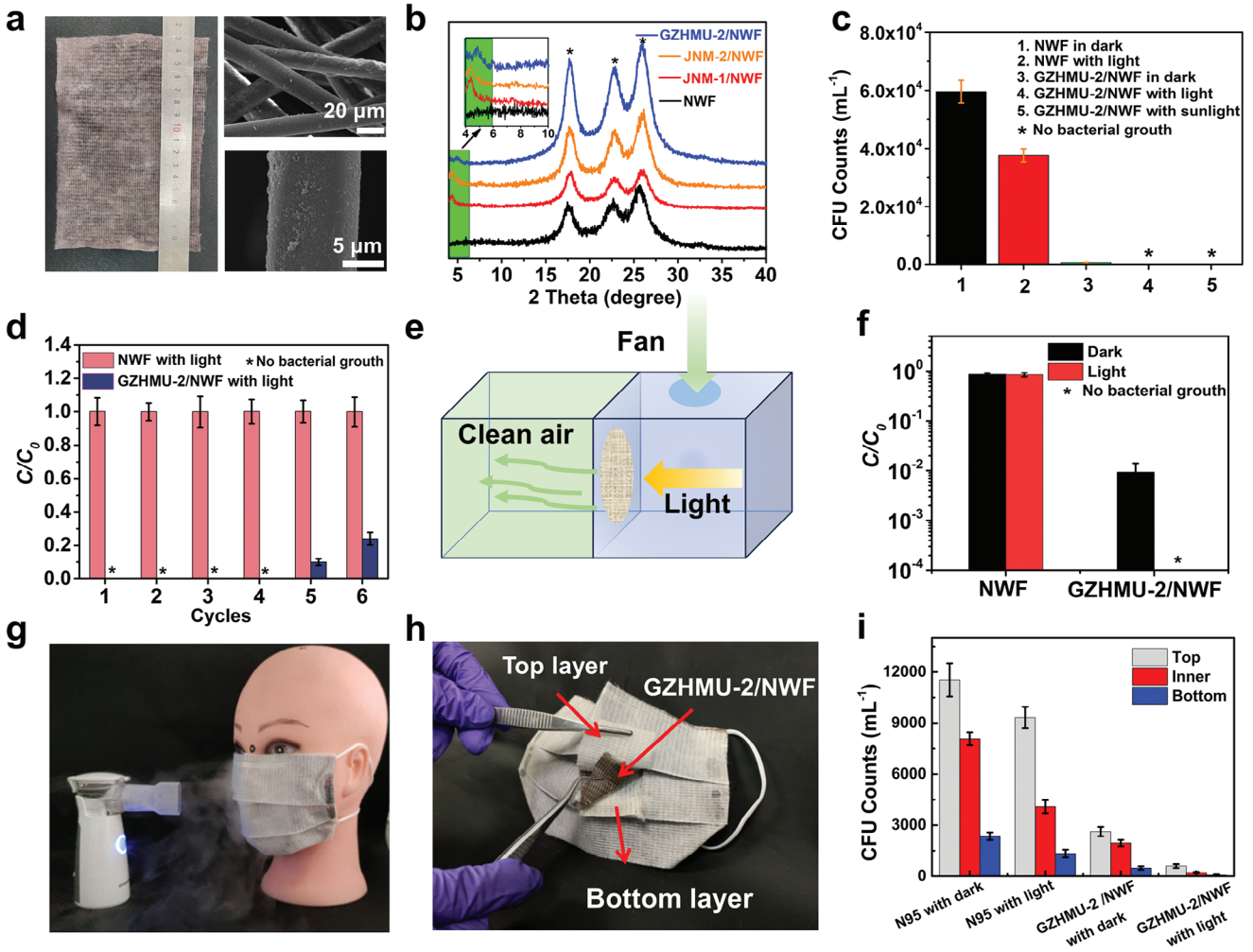

Figure 4. Photocatalytic disinfection performance of GZHMU-2/NWF. a) Optical photo and SEM images of GZHMU-2/NWF. b) PXRD patterns of GZHMU-2/NWF, JNM-1/NWF, JNM-2/NWF and pure NWF. c) Antibacterial performance comparison between GZHMU-2/NWF and NWF under dark or light conditions. d) GZHMU-2/NWF antibacterial performance for six cycles of continuous use. e) Schematic representation of the air cleaning system. f) Comparison of the air disinfection performance between GZHMU-2/NWF and NWF under light and dark conditions, respectively (NWF: non-woven fabric). g) Bioaerosol generation device. h) Optical image of each layer for GZHMU-2/NWF based mask. i) CFUs in each layer of saline eluate after the reaction of GZHMU-2/NWF-based masks and commercial N95 masks.

significantly folded, damaged, or collapsed (Figure S16, Supporting Information). Moreover, as demonstrated in the microscope images, red fluorescence of dead bacteria stained with PI can be observed with GZHMU-2 and light irradiation, illustrated the efficient antibacterial behavior of GZHMU-2 induced by light (Figure S17, Supporting Information). Importantly, no bacterial regrowth was observed after removal of GZHMU-2 and light after 2 days, demonstrate that damage to *E. coli* is irreversible (Figure S18, Supporting Information). All these above results clearly illustrated that significant photocatalytic antibacterial effects arise from the GZHMU-2.

2.4. Antibacterial Performance of GZHMU-2/NWF

Encouraged by the excellent photocatalytic and antibacterial properties of GZHMU-2, the outstanding antibacterial performance of the antibacterial film prepared by the in situ growth of GZHMU-2 on NWF was further verified. Briefly, the antibacterial film, namely GZHMU-2/NWF, was acquired by coating GZHMU-2 nanocrystals via hot pressing of GZHMU-2 precursors (TAPA and Cu_3) and PEG (M_w, 200) on NWF at 170 °C. As shown in **Figure 4a**, a piece of GZHMU-2/NWF with the size of 15 cm × 10 cm has been facilely realized, which is beneficial for various practical applications. The results of scanning electron microscope (SEM) (Figure 4a; Figure S19, Supporting Information) and PXRD (Figure 4b) further confirmed that GZHMU-2 nanoparticles have been uniformly and densely in situ formed on the fibers of NWF. The load capacity of GZHMU-2 was determined to be 0.14–0.20 mg cm^{-2} based on the weight increment of NWF before and after hot pressing (Table S4, Supporting Information). According to GB/T 30766–2014 and GB 4789.2 with slight modifications, the antibacterial performance of GZHMU-2/NWF with or without visible light irradiation was explored. As

demonstrated in Figure S20 (Supporting Information), 450 µL of *E. coli* (10^6 CFU mL^{-1}) was dropped onto a 30 × 30 mm antibacterial film. After 30 min of simulated sunlight irradiation, the GZHMU-2/NWF showed no measurable levels of adhered *E. coli* cells, demonstrating its effective photocatalytic killing abilities for *E. coli* (Figure 4c; Figure S21, Supporting Information). On the contrary, even with light, JNM-1/NWF, JNM-2/NWF, and NWF without loaded materials were severely contaminated by *E. coli* (Figures S21,S22, Supporting Information). It is worth noting that the antibacterial performance of the GZHMU-2/NWF under real sunlight irradiation is comparable to that under simulated sunlight (Figure 4c; Figure S23, Supporting Information). Of particular significance, such GZHMU-2/NWF prepared with GZHMU-2 show excellent reusability as the GZHMU-2/NWF still have sufficient antibacterial effect after it has been continuously used for five times (Figure 4d). Encouraged by these favorable results, we further investigated the effectiveness of GZHMU-2/NWF for comprehensive sterilization of air in an enclosed environment. As shown in Figure 4e and Figure S24 (Supporting Information), the self-made sterilization system was prepared by separating a sealed chamber using GZHMU-2/NWF, after injecting bio aerosols into the inlet section, the surviving bacteria were counted by exposing the collector to exhaust gas on the other chamber. The model aerosol of 10^7 CFU mL^{-1} *E. coli* suspension was atomized and injected into the self-made closed sterilization system at a flow rate of 0.2 mL min^{-1} for 5 min. Noticeably, as shown in Figure 4f and Figure S25 (Supporting Information), GZHMU-2/NWF exhibits highly efficient photocatalytic killing performance against *E. coli* dispersed in the air, and the bactericidal efficiency can reach >99.99% within 30 min, which is in sharp contrast to the poor bacteriostatic ability of NWF under light conditions (inactivation efficiency, <16%) in the control. In addition, under dark conditions, the air filtered by GZHMU-2/NWF also experiences certain bacterial contamination. This reveals that the GZHMU-2/NWF itself has a certain degree of inhibitory effect on *E. coli*, and also reflects that the retention of bacteria on the GZHMU-2/NWF can be ignored. These results vividly indicate that the excellent air sterilization ability of GZHMU-2/NWF is mainly attributed to photocatalytic bactericidal activity, rather than physical barriers and adhesion.

These results encouraged us to further investigate the subsequent antiviral effects. The photocatalytic antiviral efficiency of the synthesized GZHMU-2/NWF was examined using H9N2, HCoV-229E, and H1N1 as the model. The antiviral experiments were carried out in a biosafety level 3 (BL-3) facility in accordance with institutional biosafety requirements. The initial virus titers were determined by 50% tissue culture infective dose ($TCID_{50}$) in confluent cells in 96-well microplates. 200 µL of *virus* ($TCID_{50} = 10^6$) was dropped onto a 20 × 20 mm GZHMU-2/NWF. After 30 min of irradiation, the virus suspension treated with GZHMU-2/NWF was diluted tenfold with Dulbecco's Modified Eagle Medium medium and inoculated onto MDCK cells. After 72 h, the cytopathic effects (CPE) of the cells were recorded and the $TCID_{50}$ of each virus was calculated using the Reed-Munch method. As shown in Figure S26 (Supporting Information), the survival rate of the virus treated with GZHMU-2/NWF dramatically decreased. Excitingly, the antiviral rate of H1N1 can reach up to 92.5%. These results clearly illustrate that the GZHMU-2/NWF can be a powerful candidate toward comprehensive antibacterial and antiviral requirements in numerous enclosed environments, such as offices, homes, and public transport.

2.5. Antibacterial and In Vivo Biosafety Performance of GZHMU-2/NWF Based Mask

Inspired by the excellent photocatalytic antibacterial performance of GZHMU-2/NWF, we further proved its performance and outstanding ability in basic personal protective applications such as masks, as a proof of concept. The self-cleaning ability of GZHMU-2/NWF-based masks was evaluated by comparing them with commercial masks (N95). As shown in Figure 4g, the GZHMU-2/NWF-based mask is exposed to artificial pathogenic aerosols produced by *E. coli* suspension for 5 min. The GZHMU-2/NWF-based mask consists of three layers, similar to a sandwich structure, where the GZHMU-2/NWF serves as the sandwich layer between two layers of NWF (Figure 4h). We can see that under 30 min of simulated sunlight exposure, the number of live bacteria on each layer of the GZHMU-2/NWF-based mask significantly decreased, with almost no measurable levels of live bacteria surviving (Figure 4i; Figure S27, Supporting Information), especially at the bottom layer that direct contact with the human body. This result is very exciting as it demonstrates the excellent photocatalytic antibacterial performance of the GZHMU-2/NWF-based mask. In contrast, in the control experiment, only a small number of bacteria on the top cover of N95 masks were inactivated under light. A large number of bacteria reproduce on N95 (Figure 4i; Figure S27, Supporting Information). Obviously, the GZHMU-2/NWF-based mask has more advantages in preventing pathogens than commercial masks, ensuring its broad application prospects in protective coatings.

The biosafety of GZHMU-2/NWF based masks is crucial for their future practical applications. In order to evaluate the biosafety, evaluation experiments were conducted on C57BL/6 mice exposed to different material conditions. The mice were randomly divided into three groups: control, GZHMU-2/NWF-based mask, and GZHMU-2 material group (n = 5 for each group). As shown in Figure S28 (Supporting Information), the GZHMU-2/NWF-based mask group was obtained by raising the mice in the air environment filtered by GZHMU-2/NWF. The body weight of each mouse was recorded every day during the exposure period. As shown in Figure S29 (Supporting Information), the weight changes of mice can be negligible in response to the different conditions, indicating the good biological safety of GZHMU-2. On the third day, the lung states of mice in different groups were evaluated with Computed Tomography (CT), From the CT results, it can be seen that the lungs of each group of mice maintained good morphology (**Figure 5a**). After one week of exposure, the mice were dissected and the lung tissue was collected for identification with hematoxylin and eosin (H&E) staining and TEM. As shown in Figure 5b,c, the H&E-stained lungs images and TEM images of the GZHMU-2/NWF groups showed comparable well-defined cell morphology and no apparent pathological abnormalities compared with the control group, manifesting the safety of GZHMU-2/NWF based mask. Furthermore, blood routine tests of each group were conducted, mainly including white blood cells (WBC), red blood cells (RBC), and platelets (PLT). As

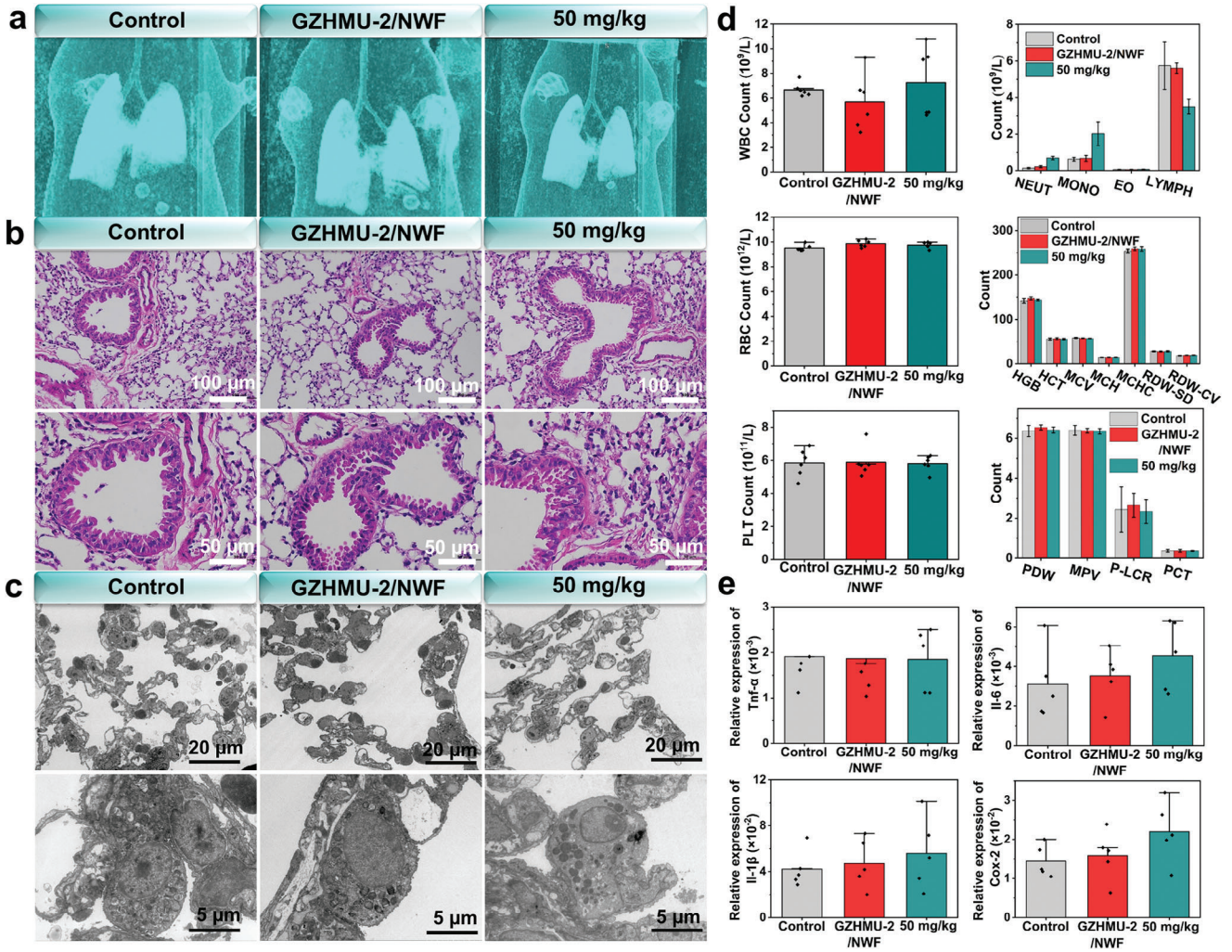

Figure 5. Biosafety analysis of GZHMU-2/NWF based mask in vivo. a) CT, b) H&E staining and c) TEM images of the lung of mice after the administration of GZHMU-2/NWF based mask and GZHMU-2 (50 mg k^{-1}g), respectively. d) Routine analysis of blood of mice after the administration of GZHMU-2/NWF based mask and GZHMU-2 (50 mg k^{-1}g) (the full names corresponding to each abbreviation are listed in Table S5, Supporting Information). e) Relative expression level of inflammatory factors (TNF) in the lung of mice after the administration of GZHMU-2/NWF based mask and GZHMU-2 (50 mg k^{-1}g) (normalized to GAPDH). Data are defined as mean ± S.D. ($n = 5$).

shown in Figure 5d, compared to the control group, there were no significant differences in RBC, WBC, and PLT between GZHMU-2/NWF and GZHMU-2 groups. Moreover, the expression levels of inflammatory genes (IL-6, IL-1β, TNF-α, COX-2) in mouse lung tissue using quantitative real-time PCR. As demonstrated in Figure 5e, there is no significant statistical difference in the expression level of IL-6, IL-1β, TNF-α, and COX-2, respectively, further confirming the biosafety. These results vividly implying that GZHMU-2/NWF with excellent biocompatibility has favorable practical application potential for personal protection.

3. Conclusion

In conclusion, we proposed a PEG-assisted solvent-free strategy to rapidly synthesize a series of donor–acceptor MCOFs under air atmosphere and further extend it via in situ hot-pressing process to prepare MCOFs based film with photocatalytic disinfect ability. Best of them, the newly designed GZHMU-2 has a wide absorption spectrum and can efficiently produce ROS under sunlight irradiation, achieving excellent photocatalytic disinfection performance. After in situ hot-pressing as a film material, the obtained GZHMU-2/NMF can effectively kill *E. coli* (99.99%), *S. aureus* (99%), and H1N1 (92.5%), meanwhile possessing good reusability. Notably, after one week, the GZHMU-2/NWF-based mask verified no obvious damage in the mice by measuring the expression of mouse blood routine, lung tissue, and inflammatory factors at the in vivo level. This work not only provides a reference for the design of high-efficiency photocatalytic personal protection films but also lays a foundation for their potentially practical applications in public health protection.

4. Experimental Section

Synthesis of GZHMU-2: Cu_3 (0.12 g, pre-synthesized according to the reference),[43] 0.40 g PTSA, 0.10 g TAPA, and 20 mL PEG (M_w, 200) were added and mixed into a three-necked flask. The device was then placed in

an oil bath and heated at 170 °C for 30 min. The resulting brown precipitate was purified by washing three times with tetrahydrofuran, DI water, and DMF, respectively. Finally, the product was dried at 60 °C under vacuum to yield GZHMU-2.

Synthesis of GZHMU-2/NWF: Cu_3 (0.12 $g_)$, 0.4 g PTSA, 0.1 g TAPA, and 20 mL PEG (Mw, 200) were mixed and sonicated. The resulting brown mixture was then loaded on a piece of NWF (15 cm × 10 cm), wrapped in aluminum foil, and then hot-pressed with an electric heating plate at 170 °C for 30 min. After washing with ethanol and drying, GZHMU-2/NMF was obtained.

Photocatalytic Disinfection Activity of MCOFs: Gram-negative *E. coli* and *S.aureus* were used as model bacteria. The bacteria were cultured for 18 h with LB broth (yeast extract 5 g L^{-1}, tryptone 10 g L^{-1}, NaCl 5 g L^{-1}) at 37 °C to yield a cell count of ≈10^9 CFU mL^{-1}. The cells were separated by centrifuging at 4000 rpm for 5 min and then resuspended in sterile saline solution (0.9% (w/v)). For the subsequent antibacterial study, the concentration of the bacteria was adjusted to 10^7 CFU mL^{-1} using 0.9% (w/v) saline solution buffer by gradient dilution method. Photocatalytic disinfection experiments were performed by adding MCOF (60 µg) catalyst into 1 mL of bacteria solution (containing 10^7 CFU mL^{-1}). Then the sample was irradiated by simulated sunlight with a hand-held 300 W Xe lamp coupled with an AM 1.5 filter (power density: 110 mW cm^{-2}). After reacting to the predetermined time, the mixture was carefully pipetted out and the residual bacterial concentration was determined by standard plate count method. The plates were cultured for 18 h at 37 °C and the number of colonies was counted with the naked eye. Control experiments were performed following the same steps in the absence of light or photocatalyts. All of the data represented mean ± S.D. from three independent measurements.

Biosafety Analysis: All C57BL/6 mice (four-six weeks) used in this study were purchased from Liaoning Changsheng biotechnology Co. Ltd. All animal experiments in this study were in accordance with the Institutional Animal Care and Use Committee of Guangzhou Medical University (G2023-069). After two weeks of adaptive feeding, C57BL/6 mice were subjected to toxicity experiments. The mice were randomly divided into three groups: control, GZHMU-2/NWF-based mask, and GZHMU-2 material group ($n = 5$ for each group). The control group was injected with 20 µL of 0.9% (w/v) saline solution through the nasal cavity into mice, and the GZHMU-2 material group was injected with 20 µL of (50 mg $k^{-1}g$) dose of GZHMU-2. The GZHMU-2/NWF-based mask group was placed the mice in an air environment filtered by raised in an air environment filtered by GZHMU-2/NWF. The body weight of each mouse was recorded every 2 days during the exposure period. On the third day, CT images of the lungs of mice were collected. After one week of exposure, the mice were anesthetized and euthanized for dissection. The blood samples were collected for routine blood examination. Additionally, the Lung tissue was obtained for H&E staining and TEM identification. Moreover, the RNA in the lung tissue of mice was extracted and reverse-transcribed. The expression levels of inflammatory genes such as Il-6, Il-1β, Tnf-α, and Cox-2 were analyzed by qRT-PCR using GoTaq qPCR Master Mix (Promega), performed with a QuantStudio5 real-time PCR system (Applied Biosystems, Foster City, California). Glyceraldehyde 3-phosphate dehydrogenase (GAPDH), a housekeeping gene, was used as an internal standard. Data were defined as mean ± S.D. ($n = 5$). The relative expression levels of each gene were analyzed using the $2^{-\Delta\Delta ct}$ method.[44] The primers are listed in Table S6 (Supporting Information).

Supporting Information

Supporting Information is available from the Wiley Online Library or from the author.

Acknowledgements

This work was supported by the National Natural Science Foundation of P. R. China (Grant No. 22001082, 22004040, 82273795, 22171139). Natural Science Foundation of Guangdong Province (No. 2023B1515020076). The authors gratefully acknowledge HZWTECH for providing computation facilities.

Conflict of Interest

The authors declare no conflict of interest.

Author Contributions

J.W., L.L., C.X., and H.J. contributed equally to this work. X.-J.H., Y.W., Y.C., and Y.-Q.L. conceived the idea. X.-J.H., J.W., and L.L. designed the experiments. L.L. and H.J. collected and analyzed the data. C.-S.X., H.J., Q.-X.X., X.-Y.Y., J.-C.L., and H.X. assisted with the experiments and characterizations. H.-X. did the DFT calculation and analysis. J.W., L.L., H.X., and X.-J.H. wrote the manuscript. All authors discussed the results and commented on the manuscript.

Data Availability Statement

The data that support the findings of this study are available from the corresponding author upon reasonable request.

Keywords

antibiosis, antiviral, hot-pressing, metal covalent organic frameworks, photocatalysis

Received: November 1, 2023
Revised: December 16, 2023
Published online:

[1] J. W. Costerton, P. S. Stewart, E. P. Greenberg, *Science* **1999**, *284*, 1318.
[2] C. Sharma, J. Bayry, *Nat. Rev. Rheumatol.* **2023**, *19*, 399.
[3] O. Mitjà, D. Ogoina, B. K. Titanji, C. Galvan, J.-J. Muyembe, M. Marks, C. M. Orkin, *Lancet* **2023**, *401*, 60.
[4] M. Talaat, B. Zayed, S. Tolba, E. Abdou, M. Gomaa, D. Itani, Y. Hutin, R. Hajjeh, *Emerging Infect. Dis.* **2022**, *28*, 717.
[5] E. Huynh, A. Olinger, D. Woolley, R. K. Kohli, J. M. Choczynski, J. F. Davies, K. Lin, L. C. Marr, R. D. Davis, *Proc. Natl. Acad. Sci. U. S. A.* **2022**, *119*, 2109750119.
[6] M. D. Ramuta, C. M. Newman, S. F. Brakefield, M. R. Stauss, R. W. Wiseman, A. Kita-Yarbro, E. J. O'connor, N. Dahal, A. Lim, K. P. Poulsen, N. Safdar, J. A. Marx, M. A. Accola, W. M. Rehrauer, J. A. Zimmer, M. Khubbar, L. J. Beversdorf, E. C. Boehm, D. Castañeda, C. Rushford, D. A. Gregory, J. D. Yao, S. Bhattacharyya, M. C. Johnson, M. T. Aliota, T. C. Friedrich, D. H. O'connor, S. L. O'connor, *Nat. Commun.* **2022**, *13*, 4717.
[7] B. J. Cowling, D. K. M. Ip, V. J. Fang, P. Suntarattiwong, S. J. Olsen, J. Levy, T. M. Uyeki, G. M. Leung, J. S. Malik Peiris, T. Chotpitayasunondh, H. Nishiura, J. Mark Simmerman, *Nat. Commun.* **2013**, *4*, 1935.
[8] Y. Cheng, N. Ma, C. Witt, S. Rapp, P. S. Wild, M. O. Andreae, U. Pöschl, H. Su, *Science* **2021**, *372*, 1439.
[9] T. R. Frieden, S. Cash-Goldwasser, *Ann. Intern. Med.* **2021**, *174*, 421.
[10] L. Wang, X. Zhang, X. Yu, F. Gao, Z. Shen, X. Zhang, S. Ge, J. Liu, Z. Gu, C. Chen, *Adv. Mater.* **2019**, *31*, 1901965.
[11] B. Ran, Z. Wang, W. Cai, L. Ran, W. Xia, W. Liu, X. Peng, *J. Am. Chem. Soc.* **2021**, *143*, 17891.
[12] H. Ou, Y. Qian, L. Yuan, H.e Li, L. Zhang, S. Chen, M. Zhou, G. Yang, D. Wang, Y. Wang, *Adv. Mater.* **2023**, *35*, 2305077.
[13] M. Yang, S. Qiu, E. Coy, S. Li, K. Zaleski, Y. Zhang, H. Pan, G. Wang, *Adv. Mater.* **2021**, *34*, 2106314.

[14] P.-Z. Wang, J.-X. Qu, H.e-S. Shao, *Bioact. Mater.* **2022**, *17*, 289.
[15] D. Ma, P. Li, X. Duan, J. Li, P. Shao, Z. Lang, L. Bao, Y. Zhang, Z. Lin, B.o Wang, *Angew. Chem., Int. Ed.* **2020**, *59*, 3905.
[16] X. Fan, F. Yang, C. Nie, L. Ma, C. Cheng, R. Haag, *Adv. Mater.* **2021**, *33*, 2100637.
[17] S. Kumaran, E. Oh, S. Han, H.-J. Choi, *Nano Lett.* **2021**, *21*, 5422.
[18] Z. Jiang, X. Xu, Y. Ma, H. S. Cho, D. Ding, C. Wang, J. Wu, P. Oleynikov, M. Jia, J. Cheng, Y.i Zhou, O. Terasaki, T. Peng, L. Zan, H. Deng, *Nature* **2020**, *586*, 549.
[19] S. Yuan, L. Feng, K. Wang, J. Pang, M. Bosch, C. Lollar, Y. Sun, J. Qin, X. Yang, P. Zhang, Q.i Wang, L. Zou, Y. Zhang, L. Zhang, Y.u Fang, J. Li, H.-C. Zhou, *Adv. Mater.* **2018**, *30*, 1704303.
[20] H.a L. Nguyen, F. Gándara, H. Furukawa, T. L. H. Doan, K. E. Cordova, O. M. Yaghi, *J. Am. Chem. Soc.* **2016**, *138*, 4330.
[21] S. Diercks Christian, M. Yaghi Omar, *Science* **2017**, *355*, eaal1585.
[22] K. Geng, T. He, R. Liu, S. Dalapati, K.e T. Tan, Z. Li, S. Tao, Y. Gong, Q. Jiang, D. Jiang, *Chem. Rev.* **2020**, *120*, 8814.
[23] F. Liu, P. Zhou, Y. Hou, H. Tan, Y. Liang, J. Liang, Q. Zhang, S. Guo, M. Tong, J. Ni, *Nat. Commun.* **2023**, *14*, 4344.
[24] J. Li, X. Jing, Q. Li, S. Li, X. Gao, X. Feng, B.o Wang, *Chem. Soc. Rev.* **2020**, *49*, 3565.
[25] D. Han, X. Liu, S. Wu, *Chem. Soc. Rev.* **2022**, *51*, 7138.
[26] Y. Zeng, R. Zou, Y. Zhao, *Adv. Mater.* **2016**, *28*, 2855.
[27] L. Zhang, G. Ng, N. Kapoor-Kaushik, X. Shi, N. Corrigan, R. Webster, K. Jung, C. Boyer, *Angew. Chem., Int. Ed.* **2021**, *60*, 22664.
[28] H.-J. Zhu, M. Lu, Y.i-R. Wang, S.u-J. Yao, M.i Zhang, Y.u-H.e Kan, J. Liu, Y. Chen, S.-L.i Li, Y.a-Q. Lan, *Nat. Commun.* **2020**, *11*, 497.
[29] X. Wang, K. Ma, T. Goh, M. R. Mian, H. Xie, H. Mao, J. Duan, K. O. Kirlikovali, A. E. B. S. Stone, D. Ray, M. R. Wasielewski, L. Gagliardi, O. K. Farha, *J. Am. Chem. Soc.* **2022**, *144*, 12192.
[30] A. Kuc, M. A. Springer, K. Batra, R. Juarez-Mosqueda, C. Wöll, T. Heine, *Adv. Funct. Mater.* **2020**, *30*, 1908004.
[31] X. Zhang, B. Wang, A. Alsalme, S. Xiang, Z. Zhang, B. Chen, *Coord. Chem. Rev.* **2020**, *423*, 213507.
[32] W.-K. Han, Y. Liu, X. Yan, Y. Jiang, J. Zhang, Z.-G. Gu, *Angew. Chem., Int. Ed.* **2022**, *61*, 202208791.
[33] L. Sun, M. Lu, Z. Yang, Z. Yu, X.i Su, Y.a-Q. Lan, L. Chen, *Angew. Chem., Int. Ed.* **2022**, *61*, 202204326.
[34] J. Zhou, J. Li, L. Kan, L. Zhang, Q. Huang, Y. Yan, Y. Chen, J. Liu, S.-L.i Li, Y.a-Q. Lan, *Nat. Commun.* **2022**, *13*, 4681.
[35] J.-N. Chang, J.-W. Shi, Q.i Li, S. Li, Y.i-R. Wang, Y. Chen, F. Yu, S.-L.i Li, Y.a-Q. Lan, *Angew. Chem., Int. Ed.* **2023**, *62*, 202303606.
[36] W. Huang, X. Wang, W. Zhang, S. Zhang, Y. Tian, Z. Chen, W. Fang, J. Ma, *Appl. Catal., B* **2020**, *273*, 119087.
[37] W. Sun, X. Tang, Q. Yang, Y.i Xu, F. Wu, S. Guo, Y. Zhang, M. Wu, Y. Wang, *Adv. Mater.* **2019**, *31*, 1903176.
[38] Y. Peng, M. Zhao, B.o Chen, Z. Zhang, Y. Huang, F. Dai, Z. Lai, X. Cui, C. Tan, H. Zhang, *Adv. Mater.* **2018**, *30*, 1705454.
[39] Y. Li, M. Karimi, Y.-N. Gong, N. Dai, V. Safarifard, H.-L. Jiang, *Matter* **2021**, *4*, 2230.
[40] M. Li, S. Qiao, Y. Zheng, Y. H. Andaloussi, X. Li, Z. Zhang, A. Li, P. Cheng, S. Ma, Y. Chen, *J. Am. Chem. Soc.* **2020**, *142*, 6675.
[41] P. Li, J. Li, X. Feng, J. Li, Y. Hao, J. Zhang, H. Wang, A. Yin, J. Zhou, X. Ma, B.o Wang, *Nat. Commun.* **2019**, *10*, 2177.
[42] S. Wang, L. Yang, K. Xu, H. Chen, N. Huang, *ACS Appl. Mater. Interfaces* **2021**, *13*, 44806.
[43] R. J. Wei, H.-G. Zhou, Z. Y. Zhang, G. H. Ning, D. Li, *CCS Chem.* **2020**, *2*, 2045.
[44] Q. Hua, Y. Liu, M. Li, Y. Chen, Q. Diao, H. Zeng, Y. Jiang, *Toxicol. Sci.* **2020**, *179*, 70.